ACS NANO

www.acsnano.org

ARTICLE

YS-TaS_2 and $Y_xLa_{1-x}S$-TaS_2 ($0 \leq x \leq 1$) Nanotubes: A Family of Misfit Layered Compounds

Simon Hettler,▽ M. B. Sreedhara,▽ Marco Serra, Sudarson S. Sinha, Ronit Popovitz-Biro, Iddo Pinkas, Andrey N. Enyashin,* Reshef Tenne,* and Raul Arenal*

Cite This: *ACS Nano* 2020, 14, 5445−5458

Read Online

ACCESS | Metrics & More | Article Recommendations | Supporting Information

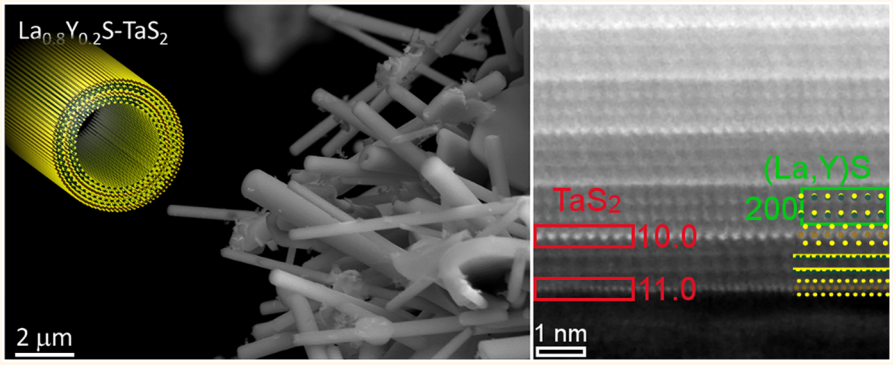

ABSTRACT: We present the analysis of a family of nanotubes (NTs) based on the quaternary misfit layered compound (MLC) $Y_xLa_{1-x}S$-TaS_2. The NTs were successfully synthesized within the whole range of possible compositions *via* the chemical vapor transport technique. In-depth analysis of the NTs using electron microscopy and spectroscopy proves the in-phase (partial) substitution of La by Y in the (La,Y)S subsystem and reveals structural changes compared to the previously reported LaS-TaS_2 MLC-NTs. The observed structure can be linked to the slightly different lattice parameters of LaS and YS. Raman spectroscopy and infrared transmission measurements reveal the tunability of the plasmonic and vibrational properties. Density-functional theory calculations showed that the $Y_xLa_{1-x}S$-TaS_2 MLCs are stable in all compositions. Moreover, the calculations indicated that substitution of La by Sc atoms is electronically not favorable, which explains our failed attempt to synthesize these MLC and NTs thereof.

KEYWORDS: *inorganic nanotubes, misfit layered compounds, electron microscopy, electron spectroscopy, Raman spectroscopy, charge transfer, density-functional theory*

The observation of fullerene-like structures and nanotubes (NTs) formed by the layered compound WS_2[1] has instigated a lot of research dedicated to inorganic nanomaterials.[2−4] Among these, misfit layered compounds (MLCs) play a special role. Microtubules based on MLCs were reported early on.[5] More recently, several solid-state strategies for the syntheses of various MLC nanotubes were described.[6−8] MLCs consist of two different layered oxides or chalcogenides that are stacked alternately along their *c* direction. In the case of chalcogenide MLCs the stacking is composed of a metal chalcogenide (MX) with a distorted rock-salt structure and a transition-metal dichalcogenide (TX_2) with hexagonal structure (see Figure 1 for a schematic presentation).[9−12] As both compounds exhibit their own symmetry, the stacking typically is incommensurate at least in one direction (*a* and/or *b*), yielding the chemical formula $(MX)_{1+y}(TX_2)_m$ [M = Sn, Pb, Sb, Bi, rare earth atoms (Ln); T = Sn, Ti, V, Cr, Nb, Ta; X = S, Se, Te; $0.08 < y < 0.32$; $m = 1, 2, 3$],[3,4] which is denoted for simplicity as MX-TX_2. The deviation from stoichiometry is calculated from the *a* lattice parameters

Received: November 23, 2019
Accepted: April 29, 2020
Published: April 29, 2020

https://dx.doi.org/10.1021/acsnano.9b09284
ACS Nano 2020, 14, 5445−5458

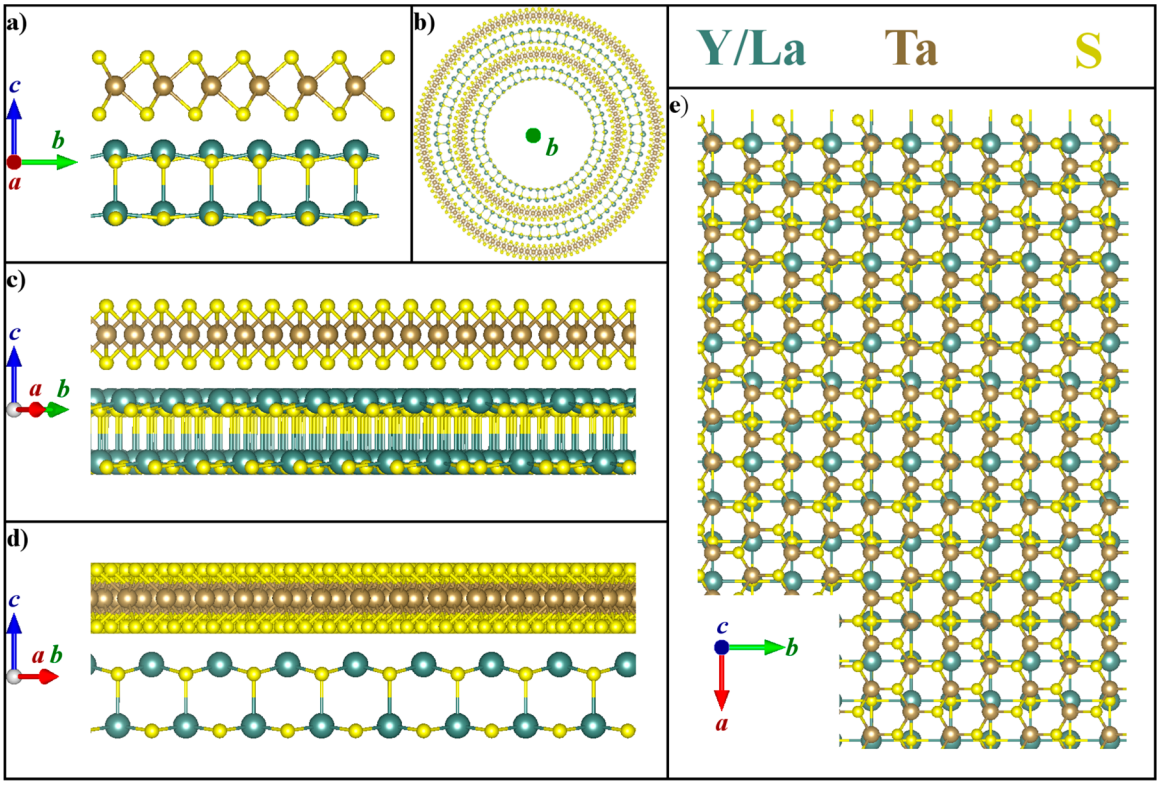

Figure 1. Schematic representation of the (Y,La)S-TaS_2 misfit structure stacked periodically along the *c*-axis depicted from different directions. (a) The view along *a* reveals that the lattices of (Y,La)S and TaS_2 have the same constant along *b*. (b) NT formed by two layers of the stack with the *b*-axis coinciding with the tube axis. Rotation of the stack in (a) around *c* by (c) 30° and (d) 45° yields the [110] projection of TaS_2 and (Y,La)S, respectively. (e) The mismatch of MX (rock-salt) and TX_2 (hexagonal) along the *a* direction is clearly visible by the view along the *c*-axis.

according to the formula $1 + y = 2a_{TX_2}/a_{MX}$. The mismatch between the MX and TX_2 layers along the *a*- and/or *b*-axis induces a strain, which is one important driving force for the formation of NTs and nanoscrolls.[13] Combining this "structural" driving force with the "chemical" one, *i.e.*, eliminating the dangling bonds of the rim atoms by folding the layer and seaming,[1,2] facilitates the formation of MLC-NTs.

MLC-NTs are promising for applications, *e.g.*, in the field of thermoelectricity, due to the complementary properties of the two layered compounds. The physical behavior of MLCs at low temperatures did not receive much attention,[14,15] let alone in their quasi-1D nanotubular form, which were reported more than a decade ago.[16,17] Recently, a modified synthetic process of MLC-NTs permitted introducing additional elements to form quaternary compounds starting from LaS-TaS_2[18] by partial replacement of La by Sr[19] in the MX sublattice or of the transition metal in the TX_2 sublattice (T = Ta, Nb).[20] Furthermore, partial replacement of the sulfur atoms by selenium atoms led to NTs of the type LaS-$TaSe_2$ with La/Ta and S/Se superlattices.[18]

Here, the synthesis and analysis of a family of MLCs, *i.e.*, $Y_xLa_{1-x}S$-TaS_2 ($0 \le x \le 1$), is described in both the bulk form and as NTs. The MLC compound $(YS)_{1.23}NbS_2$ was studied before in its bulk form,[20] but not the analogous compound with Ta as the transition metal. The aim of the present study is to control the properties of MLC-NTs, which is sought to achieve by (partially) exchanging elements in the LaS-TaS_2 structure. In case of La, Y is a suitable element due to the chemical similarities between La(S) and Y(S). The gradual exchange of La by Y provides a pathway for fine control of the MLC structure, the degree of charge transfer from the MX slab to the TX_2 layer, and the vibrational properties of the MX subunit. In return, these chemical and structural variations serve as a gauge of the free carrier density in the semimetallic TaS_2 layer and hence a tool for controlling the plasmonic wavelength of the 1D MLC nanostructures in the infrared (IR) range. This property may have relevance to future plasmonic technology in the IR range. The NTs are synthesized by chemical vapor transport (CVT) and are analyzed by electron microscopy and spectroscopy as well as Raman and Fourier transform infrared (FTIR) measurements. Density-functional theory (DFT) calculations are presented, and the stability criteria for these compounds are discussed. Interestingly, while the Y-containing MLCs are found to be stable, MLCs based on Sc are unstable and, indeed, Sc-containing MLCs could not be obtained by the CVT method. Presumably, the charge capacity of the TaS_2 layer is not sufficient for the full charge transfer from the $Sc_xLa_{1-x}S$ layer, inhibiting the formation of a stable MLC lattice in this case.

RESULTS AND DISCUSSION

Microscopic Structure and Chemical Analysis. $Y_xLa_{1-x}S$-TaS_2 NTs were successfully synthesized for yttrium fractions of $x = 0.1$ (10 at. %), 0.2, 0.4, 0.6, 0.8, 0.9, and 1, and the corresponding samples are named Y10, Y20, ..., Y100 in the following. Figure 2 shows two scanning electron microscopy (SEM) images of Y10 and Y100 samples revealing the presence of tubular structures and common byproducts of the synthetic process, *i.e.*, MLC platelets with the same composition. A

https://dx.doi.org/10.1021/acsnano.9b09284
ACS Nano 2020, 14, 5445−5458

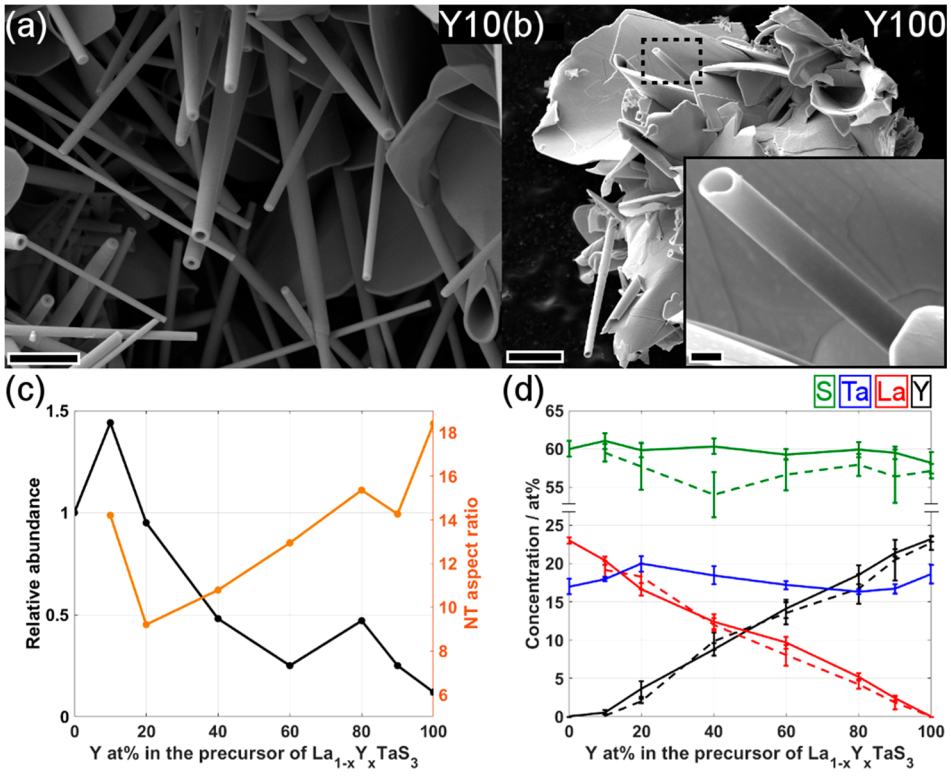

Figure 2. SEM micrographs of the tubular structures of (a) $La_{0.9}Y_{0.1}S$-TaS_2 (x = 0.1) and (b) YS-TaS_2 (x = 1) and the commonly observed byproducts. Scrolling steps of the NTs' surface can be seen in (a). Scale bars are (a) 2 μm, (b) 4 μm, and 400 nm (inset). (c) Relative abundance (by SEM analysis) and aspect ratio (by TEM analysis) of NTs as a function of Y at. % in the MS part of the precursor. (d) Concentration of the elements in at. % present in the $Y_xLa_{1-x}TaS_3$ misfit NTs as a function Y at. % in the MS part of the precursor. The analysis was done by SEM-EDS (solid lines) as well as STEM-EDS (dashed lines). The error bar at each data point corresponds to the lower and higher limits of concentrations determined in a group of at least five NTs from the same batch.

selection of SEM images of all investigated samples can be found in Figure S1, clearly revealing the successful synthesis of NTs for all values of x. The NTs appear hollow with varying length and diameter. Quantitative analysis of the relative abundance (yield) of the NTs with respect to LaS-TaS_2 (x = 0) was carried out *via* a detailed SEM analysis and is depicted in Figure 2c. While NTs are observed for all analyzed samples with different Y content, the yield of the NTs varied between the different samples. The relative abundance generally drops with increasing Y content but shows a global maximum for x = 0.1 and a second local maximum for x = 0.8. The aspect ratio (length/width) of the NTs obtained by detailed transmission electron microscopy (TEM) analysis (analysis of over 20 NTs for each sample) is shown in the same graph (orange line in Figure 2c). The aspect ratio of the NTs is the highest for x = 0 and 1, *i.e.*, the pure LaS-TaS_2 and YS-TaS_2 tubes, and shows a minimum at x = 0.2. For x > 0.2, an almost linear relationship between the aspect ratio and x is observed, which allows to control this property of the NTs in the synthetic process.

The tube widths varied between 70 and 1200 nm and the lengths between 1 and 15 μm. The average sizes of the respective NTs can be inferred from Table S1. Besides offering varying sizes, the NTs could be found in different shapes. The most common shape (>80%) is the standard tubular NT (Figure S2a), which can have a single width throughout its entire length. Alternatively, the NTs exhibit different widths, analogous to a telescope (Figure S2b). In addition to NTs, scrolls could be identified as well (Figure S2c and d).

Semiquantitative chemical analysis of the NTs was performed using energy-dispersive X-ray spectroscopy (EDS)-SEM in order to determine the atomic composition of the NTs. Figures S3–S5 show the EDS spectra of Y20, Y60, and Y100 samples. The main chemical entities La, Y, Ta, and S are observed, as well as small traces (<1 at. %) of Cl, which was used as a transport agent. Figure 2d summarizes the atomic concentration of each element as a function of Y (at. %) content in the precursor (with respect to the La content in the metal sulfide (MS) unit). This analysis reveals that the Y content in the NTs exhibits an almost linear relationship with the Y content in the precursor. It implies that Y substitutes easily the La in the MS slab without appreciable lattice distortion. This situation is entirely different from the case of Nb substitution into the Ta site of the TX_2 unit.[21] In this case, the Nb content of the MLC (and NTs) was very small up to 60 at. % Nb in the precursor. Beyond that level, the niobium substitution of the Ta in the TaS_2 of the NT lattice increased sharply. Note however that in this case the TX_2 unit of the Nb-rich NTs revealed a transformation from the 2H (hexagonal coordination) to 1T (octahedral coordination) polytype, which is quite uncommon in TaS_2-based MLC.[22,23]

In addition to SEM-EDS, chemical analysis was also performed by scanning (S)TEM-EDS for several NTs from all the samples in order to determine their average composition. Three examplary spectra are depicted in Figure S6, and the results are summarized in Table S1. The values obtained for Y, La, and S have been added as dashed lines to Figure 2d. Ta is omitted in the plot as the analyzed Ta-L edge

https://dx.doi.org/10.1021/acsnano.9b09284
ACS Nano 2020, 14, 5445−5458

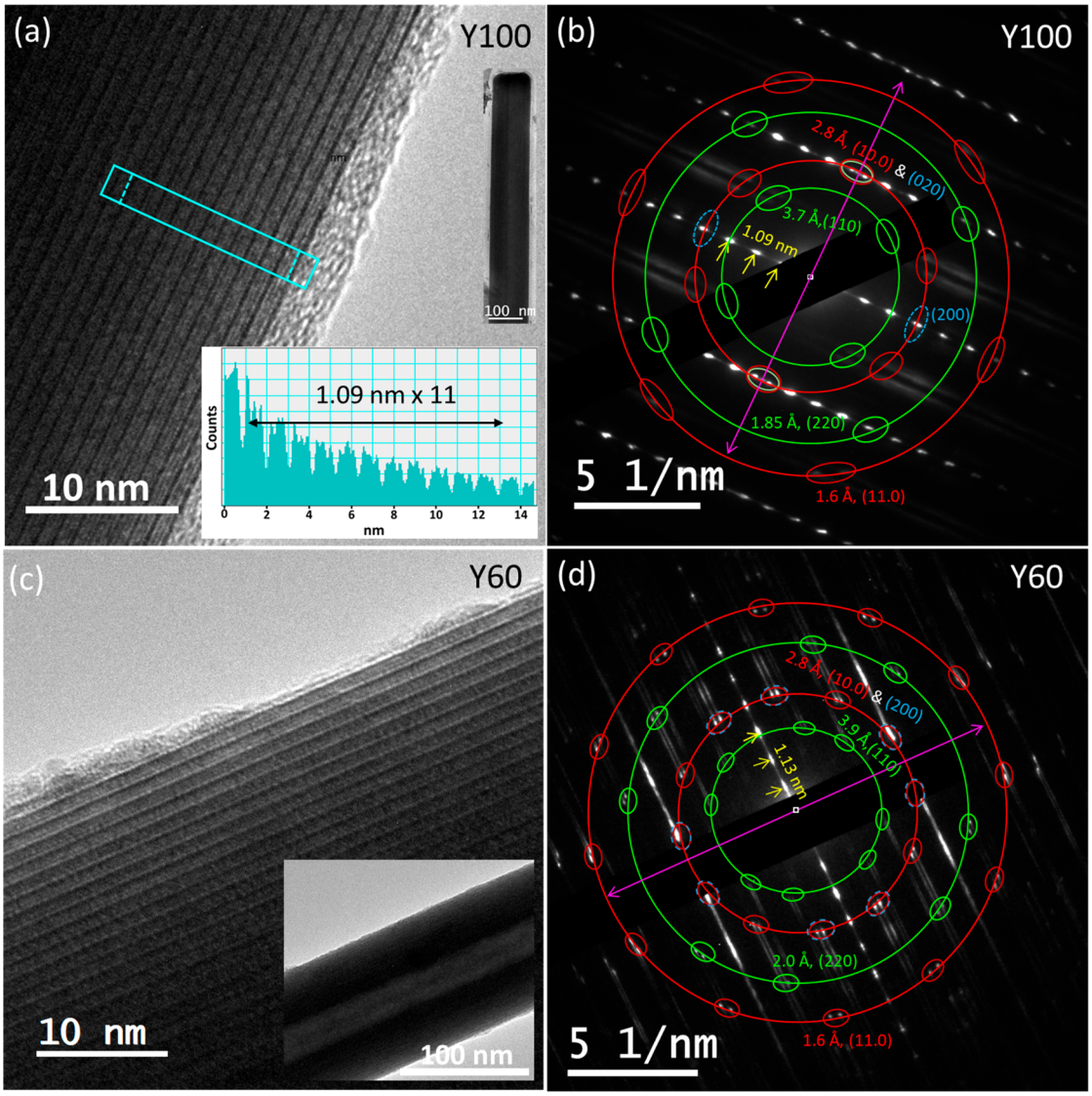

Figure 3. TEM images and corresponding SAED patterns of (a, b) YS-TaS_2 (Y100) and (c, d) $Y_{0.6}La_{0.4}S$-TaS_2 (Y60) misfit tubular structures with YS (or $Y_{0.6}La_{0.4}S$) and TaS_2 subunits periodically stacked along the *c* direction with the misfit along the *a* direction. Left panel (a, c) High-resolution and corresponding low-magnification images with intensity line profile drawn perpendicular to the tubule axis showing the periodicity of the (Y,La)S and TaS_2 structures. (b, d) SAED patterns acquired from the NTs shown in the corresponding panels. Diffraction spots corresponding to the same interplanar spacings are marked by circles (red for TaS_2 and green/blue for YS), and the respective Miller indices are marked. The basal reflections are indicated by small yellow arrows, and the tubule axis is marked by purple double arrows. The chiral angles are 7.5° (b) and 3° (d).

overlaps with the Cu−K signal stemming from the TEM support grid. The concentrations determined by this technique and their dependence on the composition (x) agree well with the results obtained by SEM-EDS (Figure 2d). Although the Y content increases linearly with x, the intended ratio between Y and La was only correctly attained for $x > 0.2$. Especially the Y/La ratio in the NTs of Y10 was found to be very low (2/98). Together with the high relative abundance of the Y10 sample, the findings suggest that the stability of LaS-TaS_2 NTs can be increased by doping with a few at. % of Y. This doping seems to be favorable in comparison to the incorporation of a considerable amount of Y (>1−2%) and the accompanying distortion of the LaS lattice due to the smaller atomic radius of Y. Although small amounts of oxygen were detected in STEM-EDS, EELS analysis showed that the actual ordered structure of the NT was not oxidized (*vide infra*). The composition of the NTs was found to be invariable along its length.

The atomic concentration of the relevant elements averaged over all samples can be used to roughly estimate the stoichiometry of the MLC family. The average concentrations are around 18 at. % Ta, 22 at. % La+Y, and 60 at. % S (Figure 2d). This detailed analysis of several NTs in each series suggests that the composition of MS-TX_2 is approximately $(Y_xLa_{1-x}S)_{1.22}TaS_2$, which is in line with the reported $YS_{1.23}NbS_2$ bulk structure.[18] Formally the ratio between the two sulfides is calculated by the relation $2a_{TaS_2}/a_{MS} = 1 + y$ (where a is the lattice constant of the binary compounds YS (LaS) and TaS_2). Using available data,[23,24] the stoichiometry of the ternary MLC is calculated to be $(YS)_{1.20}TaS_2$ and $(LaS)_{1.14}TaS_2$. Obviously, the stoichiometry $(1 + y)$ of the quaternary $(Y_xLa_{1-x}S)_{1+y}$-TaS_2 MLCs varies along the composition tie line, but the precise behavior of this transition is not known.

https://dx.doi.org/10.1021/acsnano.9b09284
ACS Nano 2020, 14, 5445−5458

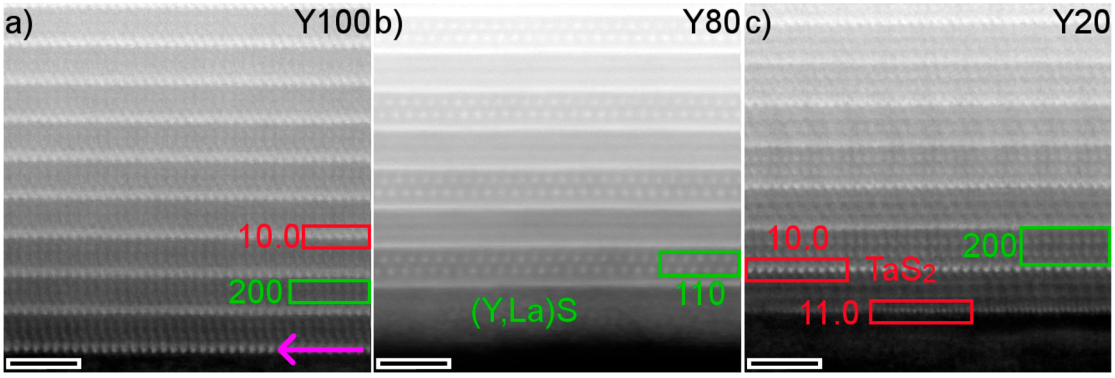

Figure 4. HAADF-STEM images of NTs from samples Y100 (a), Y80 (b), and Y20 (c). (a) The homogeneous contrast of the layers is in line with the single folding vector found by ED of the Y100 samples. (b, c) In contrast to (a), the appearance of the layer stack alternates along the *c*-axis, which is consistent with the ED patterns of such NTs revealing two folding vectors rotated by 30° with respect to each other. Identified projections of the different layers are marked in green and red for the (La,Y)S and the TaS_2 subunits, respectively. The tube axis direction is indicated by the purple arrow. The appearance of the different projections agrees with the schematics in Figure 1. Scale bars are 2 nm.

Typical TEM images and the selected area electron diffraction (SAED) patterns of pure YS-TaS_2 (Y100) are shown in Figure 3 and Figure S7. The low-magnification image of the NT (inset of Figures 3a and S7a) reveals a constant diameter of 120 nm along its entire length. Figure 3a shows the TEM image of the YS-TaS_2 superstructure, which is structurally analogous to the LaS-TaS_2 misfit structure. Here the YS and TaS_2 layers are stacked in alternating sequence along their common *c* direction. The image clearly reveals that the outermost layer of the ordered structure is TaS_2 (appearing as a dark line) and the subsequent two planes belong to the YS slab. The intensity profile of this superstructure (shown in the inset in Figure 3a) indicates that the interlayer periodicity is 1.09 nm, and this value is consistent with the interlayer spacing found in other NTs (see Figure S7). The NTs exhibit a minor amorphous shell with varying sizes below 10 nm (Figure 3a,c, Figure S7), which contains the main entities (Y(La),Ta,S) as well as carbon and is slightly oxidized. The outermost layer is clearly recognizable as TaS_2, and oxidation of the actual MLC layers was successfully prevented (as proven by EELS, *vide infra*) by keeping the contact of the NTs with air to the bare minimum.

The SAED patterns collected from the Y100 NTs are displayed in Figure 3b (also see Figure S7c,d). The intense and distinguished spots in the ED patterns indicate the good crystallinity and ordered stacking of YS-TaS_2 layers in the NT. In Figure 3b, the six pairs of spots (marked by small red circles) with the interplanar spacings of 1.6 and 2.8 Å are azimuthally equally distributed (on the red circles) and are attributed to the (11.0) and (10.0) planes of TaS_2. The four pairs of spots (marked by small green circles) with interplanar distances of 3.7 and 1.85 Å are assigned to (110) and (220) reflections of the rock-salt YS unit. The 6-fold periodicity of the hexagonal TaS_2 and the 4-fold periodicity of rock-salt YS suggest that there is a single folding vector common for both YS and TaS_2 units. This observation of a single periodicity was found for all (5) analyzed NTs of pure YS-TaS_2. The basal plane reflections indicated by the small yellow arrows show the periodicity of 1.09 nm along the *c* direction, which is perpendicular to the tube axis (marked by the purple double arrow). The 1.09 nm interlayer spacing is consistent with the one determined from the intensity line profile of the TEM image (1.09 nm, see Figure 3a). Two pairs of YS (020) and TaS_2 (10.0) reflections (marked with small green and red circles) are parallel to the tube axis. These spots reveal that the common commensurate *b*-axis coincides with the tube axis. The spots marked with the segmented small blue circles along the basal plane correspond to the YS (200) plane (see Figure S7d for a clear view) and appear azimuthally rotated by 90° with respect to the (020) spots of YS. YS (020) and (200) spots are approximately placed on the same circle and are perpendicular, which infers that the *a* and *b* lattice parameters of YS can be considered equal. In general, the NTs exhibit a high degree of crystallinity and the superstructure of the MS-TaS_2 lattice is well preserved.

Both the stacking periodicity of 1.09 nm and the interplanar distances of the YS unit (d_{110} = 3.7 Å) are several pm smaller in comparison to LaS-TaS_2 (1.15 nm/3.99 Å). This decrease of approximately 5−6% is consistent with the difference in the *a* lattice parameter between YS (0.549 nm) and LaS (0.581 nm)[23,24] induced by the smaller ionic radius of Y^{3+} (90 pm) in comparison with La^{3+} (103 pm).[25] Indeed, this seems to have considerable influence on the rock-salt lattice and, then, on the charge transfer and interlayer spacing. The smaller periodicity of YS-TaS_2 compared to LaS-TaS_2 suggests that the interlayer interactions in the former are stronger, leading to closer packing of the YS and TaS_2 layers along the *c* direction. This view is confirmed by the DFT calculations and the Raman and FTIR results (*vide infra*).

In one of the YS-TaS_2 NTs analyzed here, a stacking disorder of YS and TaS_2 layers along the *c* direction was observed and is shown in Figure S8. This kind of disorder has already been met earlier in MS-TaS_2 nanotubes.[7]

TEM images and the corresponding SAED pattern of $Y_xLa_{1-x}S$-TaS_2 NTs are shown in Figure 3c,d (x = 0.6) and in Figure S9 (x = 0.9 and 0.2). The NTs exhibit very good crystallinity irrespective of the Y content. Figure 3d shows a set of 12 (11.0) and (10.0) spots of the TaS_2 lattice and a set of eight (110) and (220) spots of the rock-salt $Y_xLa_{1-x}S$ lattice, suggesting the existence of two folding vectors in the same NT.[7] The multiplicity of these azimuthally equally distributed 12 couples of spots is six. Hence these two sets are azimuthally rotated by 30°, indicating two folding vectors for the TaS_2. Similarly, the quartets of (110) and (220) spots of $Y_xLa_{1-x}S$ (eight couples) indicate two folding vectors for the YS layers. Two folding vectors were also found for most of the NTs with

https://dx.doi.org/10.1021/acsnano.9b09284
ACS Nano 2020, 14, 5445−5458

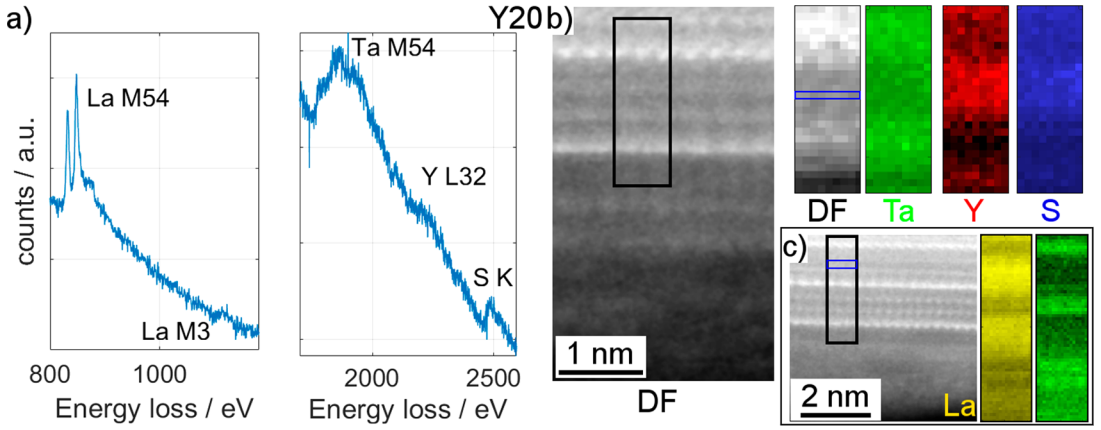

Figure 5. EELS analysis of an NT from sample Y20. (a) Spectra of the La M-edge as well as the Ta M-, Y L-, and S K-edges are taken from regions marked blue in the dark field (DF) images in b and c, respectively. (b) Ta and Y are spatially separated between the different layers recognized in the DF image. (c) La spectrum image obtained on the same NT showing enrichment of La in the two layers of MS.

different Y contents (*e.g.*, Y90, Figure S9a). One of the NTs of the Y20 sample showed two folding vectors for the TaS_2 subunit but three folding vectors for the $Y_xLa_{1-x}S$ layers, with the (200) reflections of all $Y_xLa_{1-x}S$ orientations coinciding with (10.0) spots of TaS_2 (Figure S9b). The relative orientation of the different layers of MS and TaS_2 subunits was discussed in the case of LaS-TaS_2.[7]

An analysis of the interplanar distances of both MS and TaS_2 subunits for different samples (see Table S1) reveals that while the $Y_xLa_{1-x}S$ lattice is shrinking with increasing x, the TaS_2 lattice retains its structure irrespective of the Y content. The (11.0) and (10.0) reflections of the TaS_2 subunit are always found at 1.6 and 2.8 Å, respectively, whereas the reflections attributed to the $Y_xLa_{1-x}S$ lattice are located at decreasing spatial frequencies with increasing Y content. The (110) interplanar distance decreases from 3.99 Å[18] (x = 0) to 3.9 Å (x = 0.2 and 0.6, Figure S9b and Figure 3d), 3.8 Å (x = 0.9, Figure S9a), and finally 3.7 Å (x = 1, Figure 3b). This homogeneous decrease in the MS unit goes in hand with the stacking periodicity that shows a similar behavior, changing from 1.15 nm (x = 0) to 1.09 nm (x = 1) (Table S1). These changes correspond also to the deviation from stoichiometry 1.14 for the pure La-based MLC and 1.2 in the case of yttrium. Complementary X-ray diffraction (XRD) patterns were obtained for the MLCs (NTs and platelets) in order to confirm these structural changes. The results of these analyses are displayed in Figure S10. The shift of the stacking periodicity is clearly revealed and is confirmed by the major reflections of the sublattices. The chiral angle of the NTs was found to vary between 3° and 8°. No statistically relevant dependence of the chiral angle on the Y-content of the NT was observed.

Atomic-Scale Structure and Composition Analyses. High-resolution (HR)STEM analysis of the NTs is displayed in Figure 4, which shows typical images for different NTs acquired using the high-angle annular dark field (HAADF) detector. Additional HRSTEM images can be found in Figures S11 and S12. Figure 4a reveals the homogeneous contrast of all layered stacks of a pure yttrium-based MLC, *i.e.*, Y100 NT. The atomic columns of the single layers of TaS_2 appear brighter than the double layers of Y(La)S due to the difference in atomic number Z (Z_{Ta} = 73, Z_Y = 39, Z_{La} = 57) and the fact that the intensity in HAADF images goes approximately with $Z^{1.7}$.[26,27] Evidently, the pair of YS and TaS_2 layers are coupled together and maintain a single orientation with respect to each other. This notion is confirmed by the observed projections along the [200] and the [10.0] (0.28 nm interatomic distance) direction of the respective layers, whose reflections overlap in the ED pattern (Figures 4a and 3b).

Contrary to the symmetric stacking of the layers with a single orientation in the Y0 and Y100 NTs, all other samples showed a rotation of the TaS_2 and the (La,Y)S layers (Figure 4b,c, Figures S11 and S12). ED results suggest that there exist two folding vectors for both subunits, which are rotated by 30° with respect to each other. This angle is confirmed by the image of an NT from the Y20 sample displayed in Figure 4c. The different orientations of TaS_2 in this NT can be linked to the [10.0] and [11.0] directions of TaS_2 by measuring the interatomic distances (0.28 and 0.16 nm). As these reflections encompass an angle of 30°, the adjacent layers of TaS_2 are rotated by 30° with respect to each other as expected from the ED results. As the multiplicity of the MS subsystem is four, only one of the layers of the (La,Y)S subunit coincides with a low-index zone axis. The (La,Y)S layer that is stacked on the TaS_2 layer oriented in the [10.0] direction can be identified as projection along [200] (Figure 4c), similar to the case of the Y100 NT (Figure 4a). While the two different orientations of the NT tend to alternate along the common c-axis leading to a double periodicity (Figure 4b,c, Figure S11a,b), Figure S11c,d and Figure S12c,d show that this (double periodicity) must not necessarily be the case for all the NTs. Furthermore, a disordered stacking was observed in an NT from the Y40 sample (Figure S12a,b), in which two layers of TaS_2 appeared next to each other.

The analysis presented so far suggests that La was uniformly replaced by Y in the entire volume of the investigated NTs. Results from STEM-EELS experiments on the Y20 sample conducted to ensure the in-phase replacement of La by Y are presented in Figure 5. The depicted spectrum-image (SI) analyses of the NT reveal that both the La and Y distributions show a clear enrichment in the area identified as a (La,Y)S double layer in the corresponding STEM-DF image (Figure 5b,c). In contrast, the Ta concentration is increased in the layers, which appear brighter in the corresponding STEM image. This result is in accordance with the higher contrast expected from Ta (Z = 73) with respect to La (Z = 57) and Y (Z = 39). Example spectra of the edges used for the SI analysis are shown in Figure 5a, which includes the La M-edge (832

https://dx.doi.org/10.1021/acsnano.9b09284
ACS Nano 2020, 14, 5445−5458

eV), the Ta M-edge (1735 eV), the Y L-edge (2080 eV), and the S K-edge (2472 eV). A comparison of three EELS spectra obtained from the (La,Y)S subsystem in Y100, Y60, and Y20 NTs is shown in Figure S13. The spectra have been normalized in the region before the Y L-edge located at 2080 eV to visualize the increasing intensity in the Y L-edge. Additional EELS SI analyses conducted on the Y20, Y60, and the Y100 are shown in Figures S14–S16. These results present the same spatial separation of (La,Y) and Ta between the two subunits. The spectra taken from the amorphous shell of a Y20 NT (Figure S14b) and the edge of a Y60 NT (Figure S15a) clearly show the absence of oxygen and thus the successful prevention of oxidation of the NTs achieved by avoiding prolonged contact with air. The amorphous shell of the NTs consists of the main entities as well as carbon and a minor amount of oxygen (Figure S14b). The stability of the NTs under the high electron doses necessary for the EELS experiments was found to decrease with increasing Y content (see Figure S16).

Raman Analyses. Raman analyses of lanthanide-based MLCs and their NTs were reported earlier.[7,21,28] The features in the Raman modes of these NTs can be divided into two spectral regions. The low-frequency modes from 100 to 200 cm^{-1} correspond to the phonon modes of the rock-salt (LnS) sublattice, and the phonon modes above 250 cm^{-1} originate from the TaS_2 hexagonal sublattice.[28] The rock-salt unit (LnS) exhibits two stretching lattice phonon modes A_{1g} at ∼120 and ∼150 cm^{-1} designated as RSI and RSII modes, respectively. The frequency of both modes shifts downward in energy with an increase in the mass of the rare earth element.[28] The RSI mode depends on the mass of Ln and S atoms ($M_{Ln} + M_S$), whereas the frequency of the RSII mode depends on the effective mass $\mu_{eff} = (M_{Ln} \times M_S)/(M_{Ln} + M_S)$. It is also noted that the metal atom in the TS_2 layer influences the frequency of RSI and RSII modes as observed in the case of LaS-TaS_2 and LaS-NbS_2.[21,28] The charge transfer influences the intralayer and interlayer interactions within the MLC lattices.[28] The modes corresponding to the TS_2 unit, especially the E_{2g} mode, are affected by the charge transfer from the MS to the TS_2 unit.[28,29]

Raman measurements of pure YS-TaS_2 and $(Y_xLa_{1-x}S)_{1+y}TaS_2$ (x = 0 to 1) were carried out with individual NTs in the range 100 to 500 cm^{-1} using 633 nm laser light and are shown in Figure 6 (see also Figure S17a collected using 1800 grooves/mm). Despite the large mass difference between La (139u) and Y (89u), the Raman features of YS-TaS_2 tubular crystals and its alloys are quite similar to their LaS−TaS_2 counterparts except for some dissimilarities in the YS lattice modes. However, no previous literature data is available for YS structures and YS-TaS_2 MLCs.

Regarding the low-frequency range, the samples can be divided into two categories, namely, Y contents below and above 40%. While for the Y10 and Y20 samples the Raman features follow the separation in RSI and RSII modes observed for the LaS-TaS_2 NTs, the spectrum appears significantly different for NTs with Y contents greater than 40%. In this range, a sharp peak around ∼125 cm^{-1} is seen, which is almost invariant with the Y content. In addition, instead of the sharp peak of the RSII mode in LaS-TaS_2, a broad arrangement of overlapping peaks around 150 cm^{-1} can be observed whose intensity is lower and varying with the Y content. Moreover, a peak at 178 cm^{-1} appears for YS-TaS_2, which shifts downward with reducing Y content. This particular signal is not seen in the pure LaS-TaS_2 nor in other MLC NTs of the rare-earth atoms.[7,30]

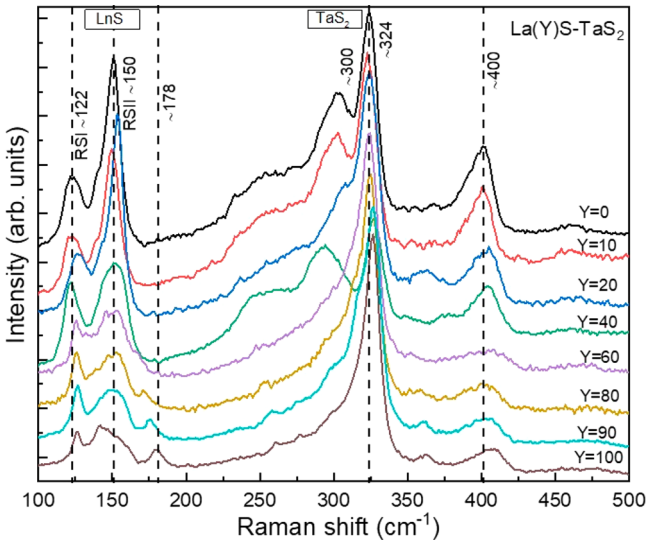

Figure 6. Raman spectra of individual $Y_xLa_{1-x}S$-TaS_2 (x = 0 to 1) NTs recorded using 633 nm laser excitation and 600 grooves/mm grating in backscattering geometry. The vertical dotted lines show the major phonon modes related to the LnS and TaS_2 subunits.

To understand further the origin of these peaks, Raman spectra with different laser excitation energies (532, 633, and 785 nm) have been acquired (Figures S17 and S18). Figure S17b shows the overlay of the Raman spectra of individual NTs with increasing Y content collected using 785 nm laser excitation. The accuracy of these measurements is higher since the spectra presented here are the average of several acquisitions, collected using an 1800 grooves/mm grating. Furthermore, this laser excitation penetrates deeper into the NT core, thereby reducing the influence of the NT surface. The peak observed at 178 cm^{-1} appears to be very prominent with the 785 nm laser excitation, and it gradually shifts downward with decreasing Y content. The broad peak at 150 cm^{-1} almost diminishes in YS-TaS_2.

A clear assignment of these low-frequency modes observed for Y contents higher than 40% is not possible without deeper analysis and theoretical support, which lies outside the scope of this work. Yet one can discuss the differences with respect to previously reported MLC structures and give possible explanations. The Raman modes are influenced by a number of properties including the changing atomic mass, the observed structural variation, and the charge transfer from the MS to the TaS_2 unit. Y is by far the lightest atom so far encountered in the MS unit of MLCs, and the appearance of modes at higher energies generally agrees with the expected shift due to the reduced mass of the Y atom. However, an estimation of the shift of the RSI and RSII modes based on their dependence on the mass and effective mass, respectively,[28] yields energies of 145 cm^{-1} (RSI) and 156 cm^{-1} (RSII) for YS-TaS_2, which disagrees with the experimental data, thereby preventing a clear assignment of the observed peaks.

In addition to the mass change, the observed structural change of the MLC NTs will affect the Raman response. The decreasing c-axis periodicity of YS-TaS_2 (1.09 nm) compared to LaS-TaS_2 (1.15 nm), concluded from the TEM/ED studies, leads to a closer packing of the lattice, in which case stronger interlayer interactions can be expected. In addition, the

https://dx.doi.org/10.1021/acsnano.9b09284
ACS Nano 2020, 14, 5445−5458

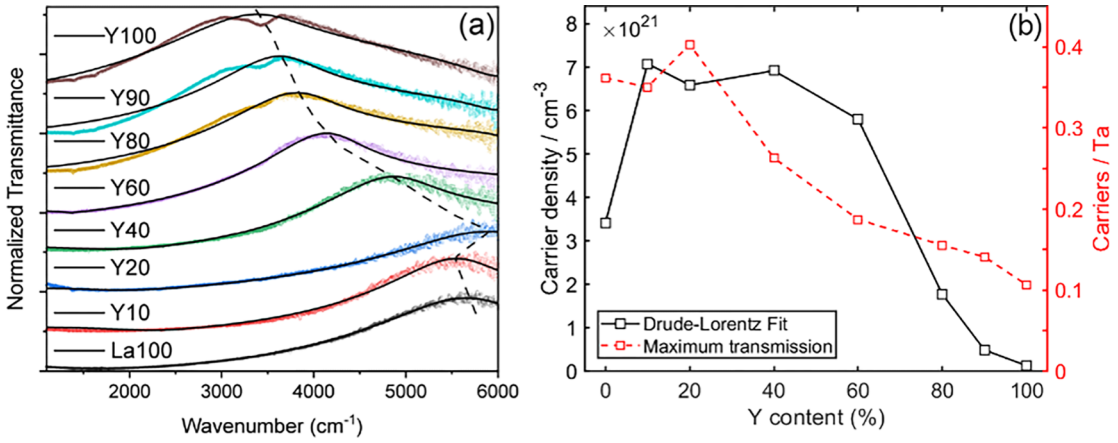

Figure 7. (a) Normalized transmission spectra of (Y_xLa_{1-x})S-TaS_2 compounds with varying Y proportions. The solid lines represent the fitted Drude−Lorentz model. The dashed line (guide to the eye) indicates the nonlinear shift of the transmittance in the spectra. (b) Variation of carrier density and carriers per Ta atom calculated from the Drude−Lorentz model (black curve) and using eq S5 (dashed red curve) as a function of Y % in the (Y_xLa_{1-x})S-TaS_2 misfit compound.

theoretically expected stoichiometry of $(YS)_{1.2}$-TaS_2 could possibly lead to a supercell along the misfit *a* direction composed of six unit cells of YS and five unit cells of TaS_2 (consider Figure 1e). In such a supercell, specific sites in the MS unit could vary energetically and favor the occupation with either La or Y atoms, leading to possible additional Raman modes. In the alloys (Y_xLa_{1-x}S-TaS_2), the lattice consists of both LaS and YS units in different proportions based on the composition. Though both crystallize in the rock-salt lattice, they have different "*a*" lattice parameters (LaS *a* = 5.81 Å and YS *a* = 5.49 Å),[23,24] which causes small lattice distortions in the mixed lattice. Given the fact that each sulfur atom has six nearest neighbor metal atoms, the local environment may vary for say six La atoms or four La and two Y atoms, *etc*. Hence the rock-salt unit is expected to have more than one kind of local vibration. Additionally, the ED and HRTEM of the NTs with mixed La and Y composition showed two distinct orientations, instead of a single orientation in the ternary MLC, at least for the outermost layers. On the other hand, the pure LaS-TaS_2 and YS-TaS_2 tubes exhibit a single orientation. The low-frequency Raman peaks of LaS-TaS_2 are relatively sharp, compared with the mixed tubes at low Y content.

The structural modulation and the valence shell configuration of the rare-earth atom in the rock-salt unit vastly affect the Raman modes of the LnS unit.[31] Previously, NTs from mixed rare-earth lattices $Ln_xLa_{(1-x)}$S-TaS_2 (Ln = Pr, Sm, Ho, Yb) were prepared and analyzed *via* Raman spectroscopy.[31] The Raman modes (A_{1g}) of the rock-salt unit of the mixed tubes exhibited a blue shift and splitting into two peaks in the case of an electronic structure with open 4f-shell (Pr, Sm, Ho) (mixed with La atoms). On the other hand, the Raman modes of the rock-salt lattice of a closed 4f-shell (Yb) atom revealed a red shift in comparison with the pure LaS-TaS_2 nanotubes. In the present case, replacing La by Y, both atoms have the same number of valence electrons; however, in contrast to the La atom, yttrium does not possess any vacant f-orbitals, which could influence the Raman signals of the two compounds. Additionally, an alteration in the charge transfer is expected, which could also influence the YS phonon modes. Furthermore, we cannot exclude a contribution from the TaS_2 unit to the low-frequency range.[7,32] In summary, a vast number of effects play into the existence of Raman peaks in the low-frequency range for MLC-NTs Y_xLa_{1-x}S-TaS_2, which requires further (theoretical) studies to allow a clear assignment of the modes. Especially polarization-dependence Raman measurements could also help further elucidate the complex Raman signature of the rock-salt sublattice of the MLC alloys.

The phonon modes around 250 to 300 cm^{-1} of LaS-TaS_2 NTs are very broad and weaker. The assignment of these modes is debatable, and they are attributed to nonlinear Raman transitions or transitions associated with defects. These phonon modes gradually disappeared as La was replaced by Y. On the other hand, the Y-rich NTs (> 40% Y) show a tiny peak around 260 cm^{-1}, which downshifts with decreasing Y content. This peak may be the manifestation of the nonlinear Raman transition related to the YS-TaS_2 structure.[28]

The Raman mode observed at 324 cm^{-1} corresponds to the E_{2g} mode of TaS_2; the large shift in this mode compared to bulk TaS_2 flakes (280 cm^{-1}) was ascribed to charge transfer from LaS to the TaS_2.[28,29] In the present case, this mode is marginally shifted to higher energies on replacing La by Y, which could be explained by a slightly modified charge transfer from the YS to TaS_2 in comparison with LaS to the TaS_2. The 400 cm^{-1} peak was assigned to the out-of-plane A_{1g} mode of TaS_2.[28] This sublattice is only weakly influenced by the Y to La exchange; indeed this peak shows some broadening and little shift, if any, replacing La by Y. The modes above 600 cm^{-1} are characteristics of oxidation products of MLC. In the present measurement, no oxidation of the NTs occurred during acquisition, though the tubes were exposed for an extended time (40 min) to the laser irradiation. The Raman spectra recorded on different NTs of the same MLC compound show similar features (Figure S19), indicating that the Raman measurements are very reproducible.

FTIR Measurements. The normalized FTIR spectra of different (Y_xLa_{1-x})S-TaS_2 compounds are displayed in Figure 7. The spectra show transmissivity in the range of about 1000 to 6000 cm^{-1} for all compounds under study with a decreasing signal-to-noise ratio upon reaching higher wave numbers. Pure TaS_2 powder did not show any signal in this range, due to the high free-carrier concentration, *i.e.*, absorption energy beyond 6000 cm^{-1}, which agrees with previous results.[33] The measured FTIR spectra clearly show that for Y contents larger

https://dx.doi.org/10.1021/acsnano.9b09284
ACS Nano 2020, 14, 5445−5458

than 20%, the maximum transmission exhibits considerable shifts to lower energies with increasing Y content. Furthermore, at high Y content the transmission spectra exhibit two nearby maxima with a tiny dip in between. The source of this splitting is not clear, suggesting two populations with different free-carrier densities. The reduced transmission in the lower energy range (<3000 cm^{-1}) is associated with free-carrier effects. In addition, the absorption in the higher energy region (less transmission) is associated with interband transitions.

The IR reflectivity of several MLCs was measured in the past.[34−36] The reflectivity threshold was attributed to the plasmon resonance of the free carriers in the misfit structure. The spectra were fitted with the Drude−Lorentz model assuming a constant effective mass of 1.0 m_0 as described in the respective section in the SI (attempts to fit the data to a pure Drude model alone were not successful).[35,37] In this model, the rock-salt unit MS is described by a Lorentzian (localized) oscillator, which contributes an electron to the Fermi sea of the free carriers in the hexagonal TS_2 unit. On the other hand, the semimetallic character of the TS_2 unit in the MLC with a half-filled $5d_{z^2}$ band is well described by free electrons, *i.e.*, the Drude model. In addition, the plasma frequency calculated from the position of the maximum in the transmission spectra (eq S5) can be used to estimate the carrier concentration and the charge transfer from MS to the TS_2 unit in the MLC compounds.[33]

Using the Drude−Lorentz model and the plasma frequency, the free carrier density in the TaS_2 layer and the amount of charge transfer from the MS to the TS_2 unit were calculated. Overall, the carrier density and thus the number of carriers per Ta atom go down with increasing Y content for both approaches (Figure 7b and Table S2) although in a nonuniform fashion. This change in the carrier density can be attributed to a modified charge transfer from the MS to the TS_2 unit. Alternatively, structural changes induced by the substitution of La by Y could induce these changes. This important point requires further investigation in future studies. Noticeably, the fitting of the Drude−Lorentz model to the lower energy part of the spectra for high-Y MLCs is not as good as for the ones with low Y content.

The rise in the free carrier density for Y10−Y40 obtained by fitting the Drude−Lorentz model (black line in Figure 7b) might result from a variation in the composition and structure of the $(Y_xLa_{1-x}S)$-TaS_2 MLC alloy that has occurred in this range. In fact, according to the EDS analyses of the NTs, the Y10 and Y20 samples were found to contain a reduced percentage of Y. For higher percentages of Y, the measured Y content corresponds with the formal content in the alloy. One possible explanation for this nonuniform behavior is that the stoichiometry of the alloy does not change continuously from 1.14 ($(LaS)_{1.14}TaS_2$) to 1.20 ($(YS)_{1.20}TaS_2$).

We are aware of the ambiguity of the fitting procedure caused by a probable change of the effective mass of the carrier upon variation of the Y content in the MLC. Nevertheless, the trend of a decreasing carrier density in the TaS_2 unit with increasing Y content is evident. A similar dependence of the plasma frequency on the Y content is observed in STEM-EELS measurement of the bulk plasmon (for details see SI, Figure S20). The determined energy of the bulk plasmon decreases from 29.3 eV (TaS_2) to 27.7 eV ($(La_{0.8}Y_{0.2}S)$-TaS_2) and 23.3 eV (YS-TaS_2), qualitatively indicating the same trend of the free carrier density in the TaS_2 slab and the charge transfer between MS and the TaS_2 unit.

In order to further investigate the electrical properties of the NTs, electrical measurements of single Y10 NTs in a dual-beam instrument (Figures S21 and S22) were conducted. The NTs were found to be semimetallic and exhibit a conductivity in the range of 10^4−10^5 S m^{-1}, which coincides with values obtained from bulk material of comparable MLCs.[34]

In summary, the experimental results from FTIR, Raman, and EELS analysis as well as the DFT calculations (*vide infra*) suggest that the charge transfer is modified by replacing La with Y. As the DFT results indicate a complex dependence of the charge carrier redistribution upon charge transfer modification, we can only speculate on the nature of the actual variation of the charge transfer from the MS to the TaS_2 unit. Nevertheless, the experimental results show that the (partial) substitution of La by Y provides a fine control over the plasmonic and vibrational properties of the NTs, which could be relevant for IR-based plasmonics using 1D devices.

Computational Results. Substitutional replacement of La by Y should lead to a change in the lattice parameter of the metal sulfide (MS) and, consequently, to a variation in the commensurability between the MS and the TaS_2 layers. DFT calculations were employed to trace a possible equilibrium between different $(Y_xLa_{1-x}S)_{1+y}TaS_2$ misfits as well as the competition between a misfit and the corresponding binary sulfides. Therefore, conveniently for both purposes the course of the enthalpy change ΔH was analyzed for the model reaction:

$$xYS + (1 - x)LaS + 1/(1 + y)TaS_2 = 1/(1 + y)(Y_xLa_{1-x}S)_{1+y}TaS_2 \quad (1)$$

ΔH was estimated as the difference in total energies between the products and the reactants, where the compounds have been considered in their solid states. According to the calculations, an increase in the yttrium content (index x) within the $(Y_xLa_{1-x}S)_yTaS_2$ misfit should enhance the relative content of the MS unit, increasing the incommensurability index y (Figure 8). Particularly, the compositions $(LaS)_{1.14}TaS_2$ and $(YS)_{1.20}TaS_2$ are found as the most favorite

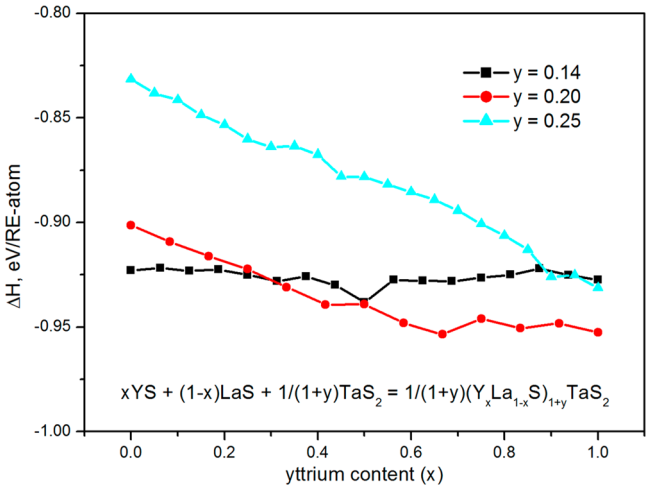

Figure 8. DFT calculation of the enthalpies of formation ΔH from binary sulfides for three misfit approximants $(Y_xLa_{1-x}S)_{1+y}TaS_2$, depending on the incommensurability factor (y) and yttrium content (x). A positive value ΔH corresponds to endothermic reaction.

https://dx.doi.org/10.1021/acsnano.9b09284
ACS Nano 2020, 14, 5445−5458

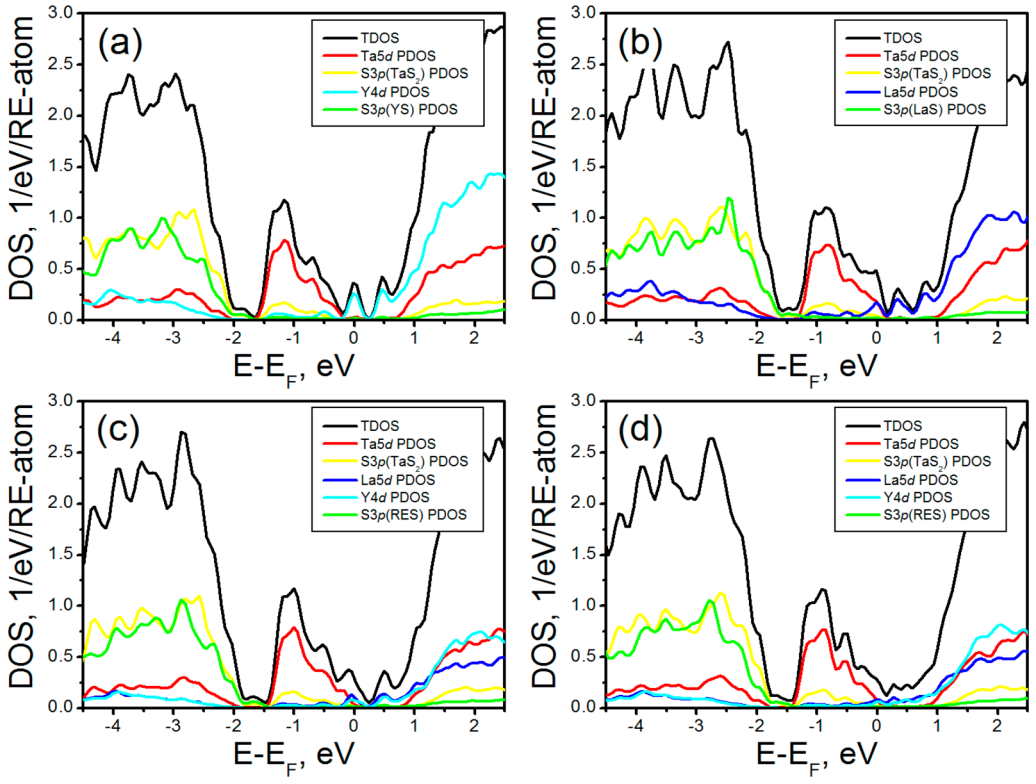

Figure 9. Electronic densities-of-states (DOS) for the misfits: (a) $(YS)_{1.20}TaS_2$, (b) $(LaS)_{1.14}TaS_2$, (c) $(Y_{0.5}La_{0.5}S)_{1.20}TaS_2$, and (d) $(Y_{0.5}La_{0.5}S)_{1.14}TaS_2$ obtained from DFT calculations.

ones among the considered ternary misfits. These findings are consistent with the experimental analysis presented above. Varying the composition (x) of the rare-earth parts within the quaternary misfits yields an almost linear variation in the relative stability for a given value of y. The dependence of ΔH on x shows different slopes for different values of the parameter y, which can have cross-points. A gradual transition from $(Y_xLa_{1-x}S)_{1.14}TaS_2$ to $(Y_xLa_{1-x}S)_{1.20}TaS_2$ can be expected over a wide range of x = 0.2−0.5 assuming a random distribution of the RE atoms. Leaving alone the entropy factor, a regular distribution of the RE atoms such as in-plane or strip-like orderings within the $(Y_{0.5}La_{0.5})$ part has little influence on ΔH, contributing about 0.01 to 0.02 eV/RE atom, respectively. Therefore, the additional entropy of mixing would favor random distribution of the RE elements in the MS lattice.

According to the calculations, all studied $(Y_xLa_{1-x}S)_{1+y}TaS_2$ misfits should have metal-like properties. The calculated electronic densities-of-states (DOS) are plotted in Figure 9 for ternary and several quaternary compounds, unveiling a close similarity in the distribution of electronic states between the different MLC compounds. The S 3p- and RE d-states responsible for the covalent RE−S bonding within MS slabs are found in the wide valence band below −1.5 eV relative to the Fermi level E_F. The band of S 3p-states responsible for covalent Ta−S bonding within the TaS_2 layers is found in the same energy region. In addition, the TaS_2 layers induce the band of localized Ta $5d_{z^2}$-states just below E_F. This localized Ta 5d-band being half-occupied in pristine 2H-TaS_2 becomes fully or almost fully occupied in the $(Y_xLa_{1-x}S)_{1+y}TaS_2$ misfits, reflecting a charge transfer from the donating $(Y_xLa_{1-x}S)$ slabs to the accepting TaS_2 layers.

In general, the DOS profiles of the studied MLC resemble a close similarity irrespective of the composition. The calculations furthermore provide evidence for a minor influence of the type of RE element in $(Y_xLa_{1-x}S)_{1+y}TaS_2$ on the occupation of the Ta $5d_{z^2}$-band, which is found almost fully occupied in comparison to that in the isolated TaS_2 layer. Indeed, the formation enthalpies ΔH of these misfits at a given y do not demonstrate extreme points, and their functions on the composition x are smooth (Figure 8). However, the origin of the metallic properties in the studied misfits can have a qualitative difference depending on the ratio between the MS and TaS_2 parts, *i.e.*, the incommensurability factor y. It plays a major role in the position of E_F, hence predetermining the lattice stability and the chemical reactivity of a misfit. Particularly, at $1 + y = 1.14$ the Fermi level is hosted mostly by the Ta $5d_{z^2}$- and S 3p-states from the TaS_2 layer (Figure 9b and d). Hence, such misfit could demonstrate an electrophilic character or a minor S deficiency, *i.e.*, excess electrons that fill the Ta $5d_{z^2}$-band. At higher $1 + y = 1.20$, the Fermi level shifts to a higher energy and can be found away from the Ta $5d_{z^2}$-band, and the density of S 3p-states gets lower until its full suppression (Figure 9a and c). Here, the main contribution to the Fermi level comes from a shallow d-band of the RE elements. Hence, in order to obtain E_F at a local DOS minimum, such misfit could act in chemical reactions in both roles, as either a nucleophilic or electrophilic agent (reducer or oxidizer).

Figure 8 shows that the most stable stoichiometry of the MLC lattice for lanthanum-rich alloys is the $1 + y = 1.14$. Indeed, the MLC lattice is not favorable for substitution of extra Y^{3+} ions, which are smaller (ionic radius of 90 pm compared to 103 pm for the La^{3+})[26] and more electronegative than the lanthanum atom. For yttrium concentrations above x = 0.3 the calculations show that the lattice with a stoichiometry $1 + y = 1.20$ becomes more stable than the 1.14 lattice. Indeed,

https://dx.doi.org/10.1021/acsnano.9b09284
ACS Nano 2020, 14, 5445−5458

the EDS analyses (see Figure 2d) show that the yttrium concentration up to $x = 0.2$ is substoichiometric; that is, it does not follow the amount of added yttrium in the precursor. According to these analyses, the yttrium concentration in the NTs increases proportionally to the amount of added yttrium in the precursor at $x = 0.3$ and above, which agrees with the calculations presented in Figure 8.

Obviously, the MS slabs within $(Y_xLa_{1-x}S)_{1.14}TaS_2$ misfits possess already the number of electrons exceeding the storage capacity of the TaS_2 layers. A further increase of y and, correspondingly, the shift of E_F into the high DOS of the conduction band would destabilize the misfit lattice. Extremely large y values could be achieved for a misfit based on MS slabs with a high atomic number per surface area, for example, using the ScS slabs. Preliminary DFT calculations on the stability of hypothetical $(ScS)_{1+y}TaS_2$ misfits suggest a minimum of ΔH at $1 + y = 1.42$. Yet, it appears to be ~0.4 eV/RE atom higher in energy than that for known $(YS)_{1.20}TaS_2$ and $(LaS)_{1.14}TaS_2$ misfits. Consequently, the existence of pristine $(ScS)_{1+y}TaS_2$ or heavily Sc-doped $(Y_xLa_{1-x}S)_{1+y}TaS_2$ misfits is highly unlikely. Indeed, as reported above, attempts to synthesize the corresponding MLCs by the CVT method used for the synthesis of $(Sc_xLa_{1-x}S)_{1+y}TaS_2$ MLC and nanotubes thereof were unsuccessful.

A functional dependence of the calculated charge transfer from the MS slab to the TaS_2 layer can be registered depending on the Y content x (Figure S23). In agreement with the electronegativities of the RE elements, the charge transfer diminishes gradually from a LaS-based misfit to its corresponding YS counterpart. The RE atoms act as the main donors of electrons here: the effective charges on La and Y atoms (+0.40e and +0.29e) within the misfit lattice are found to be more positive by 0.12−0.14e in comparison to the parent binary sulfides. The essential donation from the RE atoms can be proven also by adding vacancies in either the RE or S sublattice of the RE slab: a drastic drop of charge transfer is obtained already after introduction of single-atom RE vacancies, while the charge transfer remains insensitive to S vacancies. Expectedly from the DOS picture (Figure 9), the Ta atoms are the main acceptors of charge from the RE atoms: the charge on Ta atoms within the MLC is reduced to 0.4e in comparison with +0.5e within an isolated TaS_2 layer. Noteworthy, at any value of $(1 + y)$ the number of Ta acceptors is smaller than the number of RE donors, and the band of Ta $5d_{z^2}$-states is (almost) fully occupied for any considered misfit structure. Therefore, in the studied MLCs, the S atoms of TaS_2 act as another repository of excessive electrons from RES, either causing an increase of electron density at the interface RES||TaS_2 or even forming the dative bonding to the RE atoms at appropriate interatomic distances.[19] Both Ta and S atoms within the TaS_2 layer act as acceptors, yet, the mutual charge redistribution within the TaS_2 layer is found to have a complex character. In general, the gradual replacement of La on more electronegative Y leads to an expected electronic depletion of the S atoms within the TaS_2 subunit and to a minor benefit in electrons at Ta atoms. Comparative analysis of the atomic charges on TaS_2 atoms within the misfits and within the isolated TaS_2 layer confirms the charge saturation of Ta $5d_{z^2}$-states within MLCs at any sort of studied RE atoms (Figure S23). The electronic depletion of S(TaS_2) atoms with increasing Y content has a more pronounced character, approaching the atomic state as observed in an isolated TaS_2 layer.

According to the DOS picture and the analysis of charge distribution, the content of holes from Ta $5d_{z^2}$-states within (Y,La)S-TaS_2 misfits should be very low and almost invariant on Y content. The excessive electrons hosted at the TaS_2 layer must be considered as the charge carriers within the studied MLCs, whose content should drop at increasing Y content. The latter trend has indeed been confirmed by means of IR spectroscopy.

CONCLUSIONS

In this work, the family of misfit layered compounds $Y_xLa_{1-x}S$-TaS_2 and nanotubes thereof with different values of x ($0 \le x \le 1$) and alternating $Y_xLa_{1-x}S$ and TaS_2 layers were studied. They were prepared *via* the high-temperature chemical vapor transport technique with $TaCl_5$ as the transporting agent. The $Y_xLa_{1-x}S$-TaS_2 nanotubes were studied experimentally using different electron microscopy techniques, Raman scattering and infrared transmission studies, as well as theoretically by DFT calculations. It was found that the yttrium can occupy the lanthanum site in the MS sublattice at any value of x, but the overall concentration of the NTs in the product decreased with increasing x. Electron diffraction and HAADF-STEM analysis of pure YS-TaS_2 nanotubes showed that they exhibit a single orientation with the (commensurate) b-axis parallel to the axial growth axis of the NTs. In the quaternary $Y_xLa_{1-x}S$-TaS_2 tubes the layers mostly show two orientations rotated by 30° with respect to each other. In several cases, the nanotubes exhibited double periodicity; that is, the adjacent $Y_xLa_{1-x}S$-TaS_2 layers showed a relative rotation of 30°. The $Y_xLa_{1-x}S$ sublattice and the stacking periodicity along the c-axis was found to decrease homogeneously with increasing Y content going in hand with the smaller lattice constant of YS with respect to LaS.

A typical MLC Raman spectrum was observed for the NTs with low Y content with the two main peaks in the range of 100−150 cm^{-1} characteristic for the MS lattice and in the range of 250−400 cm^{-1} for the vibration modes of TaS_2. However, for $x > 0.4$ the Raman response changed significantly including the appearance of a peak at 178 cm^{-1} for pure YS-TaS_2. Infrared measurements revealed transmissivity peaks of the studied material in the range of 1000−6000 cm^{-1}. The position of maximum transmission, and thus the plasmon frequency, shifts to lower energies with increasing Y content. This shift is attributed to an alteration of the free charge carrier density within the MLC.

DFT calculations indicate that the $Y_xLa_{1-x}S$-TaS_2 MLCs are stable, while those of $Sc_xLa_{1-x}S$-TaS_2 were found to be unstable. Indeed, attempts to obtain these latter MLCs and NTs thereof using the present method were unsuccessful. The studied $Y_xLa_{1-x}S$-TaS_2 MLC NTs were found to be semimetallic with an experimentally measured conductivity in the range of 10^5 Sm^{-1}. The main contribution to the Fermi level comes from the Ta 5d band for low x values and from the 4d Y and 5d La bands for higher values of x.

This study extends the range of known MLC compounds and NTs thereof. The present results show that the structural, plasmonic, and vibrational properties of the $Y_xLa_{1-x}S$-TaS_2 MLC can be tuned by variation of the Y content, making them highly interesting for applications, *e.g.*, for plasmon technology in the IR range. Nevertheless, further investigations are necessary to disentangle the complex interplay between microscopical properties, *i.e.*, microstructure and charge transfer, and the observed NT responses such as the infrared transmission.

https://dx.doi.org/10.1021/acsnano.9b09284
ACS Nano 2020, 14, 5445−5458

EXPERIMENTAL/METHODS

Synthesis of $Y_xLa_{1-x}S$-TaS_2 Nanotubes. YS-TaS_2 and $Y_xLa_{1-x}S$-TaS_2 NTs were prepared by the CVT technique using evacuated quartz ampules following the well-established protocol for the synthesis of modified LaS-TaS_2 NTs. The reactants were handled under the inert atmosphere provided by a glovebox in order to prevent the oxidation of the precursors. A stoichiometric amount of Y (Sigma-Aldrich 99.9%), Ta (Alfa Aesar 99.9%), and S (Sigma-Aldrich 99.98%) were mixed in an agate mortar accordingly to the proportions 1:1:3 (19 mg, 0.13 mmol of Y(La); 25 mg, 0.13 mmol of Ta; and 13.2 mg, 0.41 mmol of S). For $Y_xLa_{1-x}S$-TaS_2 NTs, part of the Y was replaced by La (Strem Chemicals 99.9%) in a proportion ranging from 10 at. % to 90 at. %. A small amount (2 mg) of $TaCl_5$ (Sigma-Aldrich 99.99%) was used as a catalyst for the synthesis of nanotubular species. The ampule was connected to a vacuum system equipped with a rotary pump and a diffusion pump protected by a liquid N_2 trap. The quartz ampules were sealed under vacuum ($<1 \times 10^{-5}$ Torr) and transferred to a preheated vertical furnace for the annealing process. The annealing was performed in two steps using two opposite gradients of temperature under constant monitoring of the temperature inside the furnace. In the first step, the ampules were submitted to a thermal gradient formed by 350 °C at the bottom edge and 800 °C at the upper edge. After 1 h, the ampules were moved inside the bore of the furnace and exposed to an opposite temperature gradient between 857 °C at the bottom part and 400 °C at the upper part. After 6 h of high-temperature annealing, the ampules were withdrawn from the furnace and were allowed to cool to room temperature. As previously observed for modified LaS-TaS_2 nanotubes, the mass transport was negligible, and the products were accumulated in the lower (high-temperature) edge of the ampule. The product was collected and stored in a N_2 atmosphere for further analysis.

Characterization of the Nanotubes. SEM imaging was done with a Zeiss Sigma 500 model. A minute quantity of native sample was picked up by a capillary tube and dispersed on carbon tape for the SEM analysis. EDS analysis was performed with the Bruker XFlash/60 mm retractable detector. The relative abundance (yield) of the NTs was estimated by analyzing many SEM images of the product. The determined yields were based on the relative surface area occupied by the NTs compared to the area occupied by the entire product in the SEM images. Each material was synthesized three times, and at least 10 SEM images for each product were analyzed. While being only semiquantitative in nature, the overall yield did not vary appreciably from one batch (of the same material) to the other, and the relative abundance of the NTs for the different $Y_xLa_{1-x}S$-TaS_2 materials was found to be reproducible.

Four-probe electrical measurement of the NTs was conducted in a Helios 650 dual-beam instrument (Thermo Fisher Scientific) applying a focused-ion beam (FIB)-assisted transfer to the measurement chip and subsequent contacting of the NT with FIB-induced Pt deposition.

TEM and SAED pattern analyses were performed using a JEOL JEM2100 microscope operated at 200 kV. The analysis of the TEM images, including intensity profiles along the *c*-axis, and the SAED was performed with Digital Micrograph 3.1.0 (Gatan) software.

XRD patterns were obtained in a PANalytical Empyrean using the Cu Kα line. The samples were freshly prepared by drop casting of powder dispersed in ethanol on a zero-background Si substrate and subsequently analyzed in reflection mode in the range 4−90°.

Two aberration-corrected (probe and image, respectively) Titan microscopes (Thermo Fisher Scientific) were used to perform high-resolution (HR)TEM and scanning (S)TEM imaging using HAADF, annular dark field (ADF), and bright field (BF) detectors. The microscopes were operated at 300 kV and EDS and electron energy-loss spectroscopy (EELS) were applied using the probe-corrected microscope equipped with a high-brightness field emission gun (X-FEG) and respective detectors (EDAX Si(Li) detector, Gatan Tridiem ESR 865 EEL spectrometer). SAED patterns were additionally acquired using the image-corrected Titan microscope.

For HRSTEM experiments, the sample powders stored under vacuum were dispersed in ethyl alcohol. For each session, samples were freshly prepared by ultrasonication of the dispersion and drop casting of 2 μL of the dispersion onto holey carbon TEM copper grids (Quantifoil). To prevent sample contamination under the electron beam, a 14 s plasma cleaning step was implemented prior to insertion in the microscope. STEM-EDS data were analyzed using the Tia software (Thermo Fisher Scientific) and quantified with the O K-, S K-, Y K-, La L-, and Ta L-edges. EELS analysis was performed using a custom Matlab program and the La M5- (832 eV), Ta M5- (1735 eV) and Ta N23- (404 eV), Y L3- (2080 eV) and S K- (2472 eV) edges. Beam damage during EELS acquisition was observed, which increased with the Y content. ImageJ was applied for analysis of the SAED patterns. The aspect ratio of the NTs was determined by TEM analysis of over 20 images of NTs from each sample.

Raman Spectroscopy. A minute quantity of the sample was dispersed in ethanol by sonication and drop casted on the glass substrate used for the Raman analysis. Raman scattering measurements in the range from 100 to 1000 cm^{-1} were recorded on individual NTs using the backscattering mode. A LabRAM HR Evolution spectrometer (Horiba, France) equipped with different lasers and the option to manipulate the laser power was used for the analysis. For the 633 nm laser the maximum incident power on the sample was 0.225 mW. Given the spot size (1 μm) of the laser, the real incident power on the NT was ∼0.02 mW. The LabRAM is fitted with an 800 mm spectrograph with a very high spectral resolution and low stray light. Frequency calibration was performed before every measurement session using the Si peak at 520.7 cm^{-1} of single-crystalline Si(100). Initial measurements were recorded with a 600 grooves/mm grating with ∼1.8 cm^{-1} pixel resolution. Subsequently, for a detailed analysis, the measurements were done with 1800 grooves/mm grating, with a pixel resolution of ∼0.35 cm^{-1}. The NTs were illuminated using several microscope objectives (MPlanFL NA = 0.9, Olympus, Japan). The system utilizes an open confocal microscope (Olympus BXFM) with a spatial resolution better than 1 μm. Due to the very high aspect ratio of the NTs, it is very easy to visualize the single NT with a 100× objective. The Raman spectra were collected in a 1024 × 256 pixel front-illuminated CCD camera (Syncerity, Horiba, USA) with open electrode which was cooled to −60 °C. The measurements were done with the laser beam focused on a single NT at a time.

FTIR Measurements. Samples for the FTIR measurements were prepared by dispensing 2 mg of the MLC (NTs + flakes) in 100 mg of KBr powder. The mixed powders were first gently ground for homogenization and subsequently pressed into circular discs (13 mm) under a pressure of 5 tons. The discs were placed in a vacuum oven and heated to 150 °C for 18 h in order to get rid of the adsorbed water (samples that were not properly dried showed a clear footprint of water absorption). The samples were measured immediately after drying. Samples Y10 and Y20 were repeated and measured twice. The transmission spectra were recorded using a Thermo Scientific Nicolet 6700 FT-IR spectrometer with 2 cm^{-1} steps. The setup is equipped with a DTGS-KBr detector with a KBr beamsplitter and KBr disk as a reference. The FTIR chamber was purged by dry nitrogen gas during the measurements. The spectral range of this setup is 500−7400 cm^{-1} with steps of 2 cm^{-1}. The spectra were repeated for 200 scans and averaged in order to maximize the signal-to-noise level.

Computational Details. DFT calculations were performed using SIESTA 4.0 software.[38] Exchange−correlation potential was described by the generalized gradient approximation with the Perdew−Burke−Ernzerhof parametrization. The core electrons were treated within the frozen core approximation, applying norm-conserving Troullier−Martins pseudopotentials. Only valence shells were accounted for for all elements, and a double-ζ basis set was used for description of the valence orbitals. The *k*-point mesh was generated by the method of Monkhorst and Pack with a cutoff of 15 Å used for *k*-point sampling.[39] The real-space grid used for the numerical integrations was set to correspond to the energy cutoff of 300 Ry. The calculations were performed using variable-cell and atomic position relaxations, with convergence criteria corresponding to a maximum residual stress

https://dx.doi.org/10.1021/acsnano.9b09284
ACS Nano 2020, 14, 5445−5458

of 0.1 GPa for each component of the stress tensor and maximum residual force component of 0.05 eV/Å.

Preliminary test calculations of binary sulfides LaS, LaS_2, YS, YS_2, and 2H-TaS_2 revealed a good suitability of the chosen approach for describing the geometry. The differences between experimental and computed lattice parameters were found to be within ±2%. The enthalpies of formation ΔH at T = 0 K for YS, LaS, and LaS_2 from the respective elements were calculated as the difference ΔE between total energies of the compounds and the bulk elements. The theoretically calculated values −4.53 eV/YS, −5.07 eV/LaS, and −6.83 eV/LaS_2 compare very well with known experimental data for ΔH at T = 298 K: −4.77 eV/YS, −4.73 eV/LaS, and −6.46 eV/LaS_2.[40] Further, the thermodynamic stability of model misfits of the general composition $(Y_xLa_{1-x}S)_{1+y}TaS_2$ has been considered for y + 1 = 1.14, 1.20, and 1.25. The supercells of these approximants have been assembled using 16 MS and 14 TaS_2, 12 MS and 10 TaS_2, and 20 MS and 16 TaS_2 units (MS = LaS, YS), respectively.

ASSOCIATED CONTENT

Supporting Information

The Supporting Information is available free of charge at https://pubs.acs.org/doi/10.1021/acsnano.9b09284.

Additional electron microscopy, spectroscopy and diffraction data, statistical information (size, structure parameters) on the NTs, as well as Raman spectroscopy, FTIR, and DFT results (PDF)

AUTHOR INFORMATION

Corresponding Authors

Andrey N. Enyashin − *Institute of Solid State Chemistry UB RAS, 620990 Ekaterinburg, Russian Federation; Institute of Natural Sciences and Mathematics, Ural Federal University, 620083 Ekaterinburg, Russian Federation;* orcid.org/0000-0001-6195-7971; Email: enyashin@ihim.uran.ru

Reshef Tenne − *Department of Materials and Interfaces, Weizmann Institute of Science, Rehovot 76100, Israel;* orcid.org/0000-0003-4071-0325; Email: reshef.tenne@weizmann.ac.il

Raul Arenal − *Instituto de Nanociencia de Aragón, Universidad de Zaragoza, 50018 Zaragoza, Spain; Instituto de Ciencias de Materiales Aragón, CSIC-U. Zaragoza, 50009 Zaragoza, Spain; ARAID Foundation, 50018 Zaragoza, Spain;* orcid.org/0000-0002-2071-9093; Email: arenal@unizar.es

Authors

Simon Hettler − *Instituto de Nanociencia de Aragón, Universidad de Zaragoza, 50018 Zaragoza, Spain*

M. B. Sreedhara − *Department of Materials and Interfaces, Weizmann Institute of Science, Rehovot 76100, Israel;* orcid.org/0000-0003-4925-4346

Marco Serra − *Department of Materials and Interfaces, Weizmann Institute of Science, Rehovot 76100, Israel; Department of Physical Chemistry, Center for Biomedical Research (CINBIO), Universidad de Vigo, 36310 Vigo, Spain*

Sudarson S. Sinha − *Department of Materials and Interfaces, Weizmann Institute of Science, Rehovot 76100, Israel*

Ronit Popovitz-Biro − *Department of Materials and Interfaces, Weizmann Institute of Science, Rehovot 76100, Israel*

Iddo Pinkas − *Department of Chemical Research Support, Weizmann Institute of Science, Rehovot 76100, Israel;* orcid.org/0000-0001-7434-9844

Complete contact information is available at: https://pubs.acs.org/10.1021/acsnano.9b09284

Author Contributions

▽S. Hettler and M. B. Sreedhara contributed equally.

Notes

The authors declare no competing financial interest.

ACKNOWLEDGMENTS

A.E. acknowledges the support by Act 211 Government of the Russian Federation, Contract No. 02.A03.21.0006. The support of the Israel Science Foundation (Grant No. 7130970101), Irving and Cherna Moskowitz Center for Nano and Bio-Nano Imaging, and the Perlman Family Foundation and the Kimmel Center for Nanoscale Science (Grant No. 43535000350000) is greatly acknowledged. The HRSTEM and EELS studies as well as some of the ED and TEM investigations were conducted at the Laboratorio de Microscopias Avanzadas, Instituto de Nanociencia de Aragon, Universidad de Zaragoza, Spain. We thank G. Antorrena and L. Casado (LMA-INA) for their help with the XRD acquisition and the electrical measurements, respectively. R.A. gratefully acknowledges the support from the Spanish Ministry of Economy and Competitiveness (MINECO) through Project Grant MAT2016-79776-P (AEI/FEDER, UE) and from the European Union H2020 program "ESTEEM3" (823717). S.H. acknowledges funding by the German Research Foundation (HE 7675/1-1). I.P. is the incumbent of the Sharon Zuckerman Research Fellow Chair.

DEDICATION

This work is dedicated to Prof. C. N. R. Rao, a scholar and mentor, on the occasion of his 85th birthday.

REFERENCES

(1) Tenne, R.; Margulis, L.; Genut, M.; Hodes, G. Polyhedral and Cylindrical Structures of Tungsten Disulphide. *Nature* **1992**, *360*, 444−446.

(2) Tenne, R. Inorganic Nanotubes and Fullerene-Like Nanoparticles. *Nat. Nanotechnol.* **2006**, *1*, 103−111.

(3) Višić, B.; Panchakarla, L. S.; Tenne, R. Inorganic Nanotubes and Fullerene-like Nanoparticles at the Crossroads between Solid-State Chemistry and Nanotechnology. *J. Am. Chem. Soc.* **2017**, *139*, 12865−12878.

(4) Serra, M.; Arenal, R.; Tenne, R. An Overview of the Recent Advances in Inorganic Nanotubes. *Nanoscale* **2019**, *11*, 8073−8090.

(5) Bernaerts, D.; Amelinckx, S.; van Tendeloo, G.; van Landuyt, J. Microstructure and Formation Mechanism of Cylindrical and Conical Scrolls of the Misfit Layer Compounds PbNbnS2n+1. *J. Cryst. Growth* **1997**, *172*, 433−439.

(6) Radovsky, G.; Popovitz-Biro, R.; Staiger, M.; Gartsman, K.; Thomsen, C.; Lorenz, T.; Seifert, G.; Tenne, R. Synthesis of Copious Amounts of SnS2 and SnS2/SnS Nanotubes with Ordered Superstructures. *Angew. Chem., Int. Ed.* **2011**, *50*, 12316−12320.

(7) Radovsky, G.; Popovitz-Biro, R.; Lorenz, T.; Joswig, J.-O.; Seifert, G.; Houben, L.; Dunin-Borkowski, R. E.; Tenne, R. Tubular Structures from the LnS−TaS 2 (Ln = La, Ce, Nd, Ho, Er) and LaSe−TaSe 2 Misfit Layered Compounds. *J. Mater. Chem. C* **2016**, *4*, 89−98.

(8) Panchakarla, L. S.; Radovsky, G.; Houben, L.; Popovitz-Biro, R.; Dunin-Borkowski, R. E.; Tenne, R. Nanotubes from Misfit Layered Compounds. *J. Phys. Chem. Lett.* **2014**, *5*, 3724−3736.

(9) Wiegers, G. A. Misfit Layer Compounds. *Prog. Solid State Chem.* **1996**, *24*, 1−139.

(10) Grippa, A. Y.; Lidin, S.; D'yachenko, O. G.; Rupasov, D. P.; Antipov, E. V. Synthesis and Study of Sr-substituted Misfit Layer Sulfides. *Mater. Res. Bull.* **2005**, *40*, 79−91.

(11) Meerschaut, A.; Moëlo, Y.; Cario, L.; Lafond, A.; Deudon, C. Charge Transfer in Misfit Layer Chalcogenides, [(MX) n] 1+x (TX 2) m. *Mol. Cryst. Liq. Cryst. Sci. Technol., Sect. A* **2000**, *341*, 1−8.
(12) Roesky, R.; Meerschaut, A.; van der Lee, A.; Rouxel, J. Structural Study of a Niobium-Lanthanum Sulfide Compound [(Nb1−xLaxS)NbS2, x≈0.3; The First "Self-Misfit" Compound]. *Mater. Res. Bull.* **1994**, *29*, 1149−1155.
(13) Pauling, L. The Structure of the Chlorites. *Proc. Natl. Acad. Sci. U. S. A.* **1930**, *16*, 578−582.
(14) Mitchell, K.; Somers, R. C.; Huang, F. Q.; Ibers, J. A. Syntheses, Structure, and Magnetic Properties of Several LnYbQ3 Chalcogenides, Q = S, Se. *J. Solid State Chem.* **2004**, *177*, 709−713.
(15) Meerschaut, A.; Rabu, P.; Rouxel, J.; Monceau, P.; Smontara, A. Structural Reinvestigation of (LaS)1.14NbS2 and Resistivity Measurements. *Mater. Res. Bull.* **1990**, *25*, 855−861.
(16) Ohno, Y. Lamellar and Filament-Like Crystals of Misfit-Layer Compounds Containing (Sm, Ta, S) and (Pb, Bi, Nb, S) Elements. *J. Solid State Chem.* **2005**, *178*, 1539−1550.
(17) Hong, S. Y.; Popovitz-Biro, R.; Prior, Y.; Tenne, R. Synthesis of SnS2/SnS Fullerene-Like Nanoparticles. *J. Am. Chem. Soc.* **2003**, *125*, 10470−10474.
(18) Lajaunie, L.; Radovsky, G.; Tenne, R.; Arenal, R. Quaternary Chalcogenide-Based Misfit Nanotubes LnS(Se)-TaS(Se)2 (Ln = La, Ce, Nd, and Ho). *Inorg. Chem.* **2018**, *57*, 747−753.
(19) Serra, M.; Anumol, E. A.; Stolovas, D.; Pinkas, I.; Joselevich, E.; Tenne, R.; Enyashin, A.; Deepak, F. L. Synthesis and Characterization of Quaternary La(Sr)S-TaS2Misfit-Layered Nanotubes. *Beilstein J. Nanotechnol.* **2019**, *10*, 1112−1124.
(20) Rabu, P.; Meerschaut, A.; Rouxel, J.; Wiegers, G. A. The Crystal Structure of the Misfit Layer Compound (YS)1.23NbS2. *J. Solid State Chem.* **1990**, *88*, 451−458.
(21) Stolovas, D.; Serra, M.; Popovitz-Biro, R.; Pinkas, I.; Houben, L.; Calvino, J. J.; Joselevich, E.; Tenne, R.; Arenal, R.; Lajaunie, L. Nanotubes from the Misfit Compound Alloy LaS-Nb x Ta (1−x) S 2. *Chem. Mater.* **2018**, *30*, 8829−8842.
(22) Radovsky, G.; Popovitz-Biro, R.; Tenne, R. Nanotubes from the Misfit Layered Compounds MS−TaS 2, Where M = Pb, Sn, Sb, or Bi. *Chem. Mater.* **2014**, *26*, 3757−3770.
(23) Meetsma, A.; Wiegers, G. A.; Haange, R. J.; Boer, J. L. de. Structure of 2H-TaS2. *Acta Crystallogr., Sect. C: Cryst. Struct. Commun.* **1990**, *46*, 1598−1599.
(24) Hulliger, F.; Hull, G. W. Superconductivity in Rocksalt-Type Compounds. *Solid State Commun.* **1970**, *8*, 1379−1382.
(25) Shannon, R. D. Revised Effective Ionic Radii and Systematic Studies of Interatomic Distances in Halides and Chalcogenides. *Acta Crystallogr., Sect. A: Cryst. Phys., Diffr., Theor. Gen. Crystallogr.* **1976**, *32*, 751−767.
(26) Pennycook, S. J.; Nellist, P. D. Scanning Transmission Electron Microscopy. In *Imaging and Analysis*; Springer: New York, NY, 2011.
(27) *Advanced Transmission Electron Microscopy*; Deepak, F. L., Mayoral, A., Arenal, R., Eds.; Springer International Publishing: Cham, Switzerland, 2015; pp 11−14.
(28) Kisoda, K.; Hangyo, M.; Nakashima, S.; Suzuki, K.; Enoki, T.; Ohno, Y. Raman Scattering from Misfit Layer Compounds (RS) x TaS 2 (R Identical to La,Ce,Sm or Gd; S Identical to Sulphur; x Approximately = 1.2). *J. Phys.: Condens. Matter* **1995**, *7*, 5383−5393.
(29) Staiger, M.; Bačić, V.; Gillen, R.; Radovsky, G.; Gartsman, K.; Tenne, R.; Heine, T.; Maultzsch, J.; Thomsen, C. Raman Spectroscopy of Intercalated and Misfit Layer Nanotubes. *Phys. Rev. B: Condens. Matter Mater. Phys.* **2016**, *94*, 35430.
(30) Serra, M.; Stolovas, D.; Houben, L.; Popovitz-Biro, R.; Pinkas, I.; Kampmann, F.; Maultzsch, J.; Joselevich, E.; Tenne, R. Synthesis and Characterization of Nanotubes from Misfit (LnS)1+y TaS2 (Ln = Pr, Sm, Gd, Yb) Compounds. *Chem. - Eur. J.* **2018**, *24*, 11354−11363.
(31) Serra, M.; Lajaunie, L.; Sreedhara, M. B.; Miroshnikov, Y.; Pinkas, I.; Calvino, J. J.; Enyashin, A. N.; Tenne, R. Quaternary LnxLa(1-x)S-TaS2 Nanotubes (Ln = Pr, Sm, Ho, and Yb) as a Vehicle for Improving the Yield of Misfit Nanotubes. *Appl. Mater. Today* **2020**, *19*, 100581.
(32) Hirata, T.; Ohuchi, F. S. Temperature Dependence of The Raman Spectra of 1T-TaS2. *Solid State Commun.* **2001**, *117*, 361−364.
(33) Parkin, S. S. P.; Beal, A. R. 3D Transition Metal Intercalates of the Niobium and Tantalum Dichalcogenides. *Philos. Mag. B* **1980**, *42*, 627−642.
(34) Ruscher, C. H.; Haas, C.; van Smaalen, S.; Wiegers, G. A. Investigation of the Optical Reflectivity of Misfit Layer Compounds. *J. Phys.: Condens. Matter* **1994**, *6*, 2117−2128.
(35) Hangyo, M.; Nishio, T.; Nakashima, S.; Ohno, Y.; Terashima, T.; Kojima, N. Raman and Infrared Spectra of Misfit Layer Compounds MNbS3 (M = Sn, Pb, La, Ce). *Jpn. J. Appl. Phys.* **1993**, *32*, 581−583.
(36) Hangyo, M.; Kisoda, K.; Nishio, T.; Nakashima, S.; Terashima, T.; Kojima, N. Staging and Interlayer Interaction in the Misfit-Layer Compounds (RS)nNbS2 (R = La,Ce; n = 0.6,1.2) studied by Raman and Infrared Spectroscopies. *Phys. Rev. B: Condens. Matter Mater. Phys.* **1994**, *50*, 12033−12043.
(37) Wooten, F. *Optical Properties of Solids*; Elsevier Science: Burlington, 1972.
(38) Ordejón; Artacho; Soler. Self-Consistent Order-N Density-Functional Calculations for Very Large Systems. *Phys. Rev. B: Condens. Matter Mater. Phys.* **1996**, *53*, R10441−R10444.
(39) Moreno; Soler. Optimal Meshes for Integrals in Real- and Reciprocal-Space Unit Cells. *Phys. Rev. B: Condens. Matter Mater. Phys.* **1992**, *45*, 13891−13898.
(40) Franke, P.; Neuschütz, D. Binary Systems. Part 3. In *Binary Systems from Cs-K to Mg-Zr*; Springer-Verlag: Berlin/Heidelberg, 2005.

https://dx.doi.org/10.1021/acsnano.9b09284
ACS Nano 2020, 14, 5445−5458